

The Detonation Mechanism of the Pulsationally-Assisted Gravitationally-Confined Detonation Model of Type Ia Supernovae

G. C. Jordan IV,^{1,2} C. Graziani,^{1,2} R. T. Fisher,³ D. M. Townsley,⁴ C. Meakin,^{5,6}

K. Weide,^{1,2} L. B. Reid,^{7,8} J. Norris,¹ R. Hudson,¹ D. Q. Lamb,^{1,2,9}

Received _____; accepted _____

¹Flash Center For Computational Science, The University of Chicago, Chicago, IL 60637.

²Department of Astronomy and Astrophysics, The University of Chicago, Chicago, IL 60637.

³University of Massachusetts Dartmouth, Department of Physics, 285 Old Westport Road, North Dartmouth, 02740.

⁴Department of Physics and Astronomy, The University of Alabama, Tuscaloosa, AL 35487.

⁵Steward Observatory, University of Arizona, Tucson, AZ 85721.

⁶Theoretical Division, Los Alamos National Laboratory, Los Alamos, NM 87545.

⁷Western Australian Geothermal Centre of Excellence, CSIRO CESRE, Kensington, WA 6151 Australia

⁸School of Environmental Systems Engineering, University of Western Australia, Crawley WA 6009 Australia

⁹Enrico Fermi Institute, The University of Chicago, Chicago, IL 60637.

ABSTRACT

We describe the detonation mechanism comprising the “Pulsationally Assisted” Gravitationally Confined Detonation (GCD) model of Type Ia supernovae (SNe Ia). This model is analogous to the previous GCD model reported in Jordan et al. (2008); however, the chosen initial conditions produce a substantively different detonation mechanism, resulting from a larger energy release during the deflagration phase. The resulting final energy releases and ^{56}Ni yields conform better to observational values than is the case for the “classical” GCD models. In the present class of models, the ignition of a deflagration phase leads to a rising, burning plume of ash. The ash breaks out of the surface of the white dwarf, flows laterally around the star, and converges on the collision region at the antipodal point from where it broke out. The amount of energy released during the deflagration phase is enough to cause the star to rapidly expand, so that when the ash reaches the antipodal point, the surface density is too low to initiate a detonation. Instead, as the ash flows into the collision region (while mixing with surface fuel) the star reaches its maximally expanded state and then contracts. The stellar contraction acts to increase the density of the star, including the density in the collision region. This both raises the temperature and density of the fuel-ash mixture in the collision region and ultimately leads to thermodynamic conditions that produce a detonation. We demonstrate this mechanism with three 3-dimensional (3D), full star simulations of this model using the FLASH code, varying the initial offset of the ignition points for each model. The simulations are characterized by nuclear energy releases ranging from 38% to 78% of the binding energy of the white dwarf during the deflagration phase. We show that the conditions for detonation are achieved in all three of the models.

Subject headings: hydrodynamics — nuclear reactions, nucleosynthesis, abundances
— supernovae:general — white dwarfs

1. Introduction

The discovery of the accelerated expansion of the universe using Type Ia supernovae (SNe Ia) (Riess et al. 1998; Perlmutter et al. 1999) has stimulated a tremendous amount of interest in the use of SNe Ia events as standard cosmological candles, allowing them to serve as probes of the equation of state of dark energy, as parameterized by the EOS parameter $w = P/\rho$. The main challenge to the enterprise of measuring $w(z)$ using SNe Ia is reducing the systematic errors in the accuracy with which such supernovae can be used as standard candles (Dark Energy Task Force 2006). The accuracy must be improved from the current level of about 15% to about 1% in order for large surveys to determine the values of $w(z = 0)$ and its rate of change with z to better than 10% (Kim et al. 2004). The best hope for improvements in distance modulus accuracy is more accurate modeling of SNe Ia explosions.

The leading mechanism for SNe Ia explosions is the single-degenerate model in which a progenitor white dwarf accretes material from a non-degenerate companion star (Whelan & Iben 1973; Nomoto 1982), though the double-degenerate channel (Webbink 1984; Iben & Tutukov 1984) has recently received revived attention from both observation (eg, Maoz et al. (2010)) and theory (eg, van Kerkwijk et al. (2010); Zhu et al. (2011)). However, while computational models have explored prompt detonations in near-equal mass super-Chandrasekhar mergers (Pakmor et al. 2010, 2011) and head-on collisions of binary white dwarf systems (Raskin et al. 2009; Rosswog et al. 2009) it remains unclear whether more commonplace mergers between two typical C/O white dwarfs of masses $\sim 0.6M_{\odot}$ will result in a Type Ia explosion. Previous one-dimensional theoretical models suggest that such mergers will result in deflagration wave that sets off an accretion-induced collapse to a neutron star (Nomoto & Kondo 1991; Saio & Nomoto 1998, 2004; Shen et al. 2011).

The single-degenerate scenario of SNe Ia consists of an accreting white dwarf star,

with a mass near the Chandrasekhar limit, that manages to release enough nuclear energy by fusing C and O into radioactive Ni and other lighter α -elements in the time span of a few seconds or less (Nomoto et al. 1984). This rapid fusion process deposits approximately 10^{51} ergs of energy, unbinding the star and accelerating the stellar material to speeds of thousands of kilometers per second (Branch et al. 1982). This rapid fusion process must proceed in two phases (Niemeyer & Woosley 1997; Röpke et al. 2007a). The first phase begins with the initiation of a subsonic nuclear burning front (referred to as a deflagration or flame). The deflagration burns from the core of the star to the outer layers. The second phase consists of a supersonic burning front — a detonation — that consumes the remainder of the white dwarf. The transition from the deflagration phase to the detonation phase is poorly understood, and has been the subject of much modeling research. A variety of models incorporates the scenario of a deflagration followed by a detonation, such as the deflagration-to-detonation transition (DDT) (Khokhlov 1991; Gamezo et al. 2004, 2005), the pulsating reverse detonation (PRD) (Bravo & García-Senz 2009; Bravo et al. 2009), or the gravitationally confined detonation GCD (Jordan et al. 2008, 2009; Meakin et al. 2009; Townsley et al. 2007). These models differ primarily in the method by which the deflagration leads to a detonation.

In this work we use the FLASH code (Fryxell et al. 2000; Dubey et al. 2009) to extend the set of 3D whole-star GCD models in Jordan et al. (2008) (hereafter J08) to include multiple ignition points as initial conditions. These initial conditions provide more burning, and hence more energy release during the deflagration phase. The purpose of this work is to study the onset of the detonation in these models. To distinguish between the two versions of GCD models we refer to the previous body of GCD models (Townsley et al. (2007), J08, Meakin et al. (2009), and references therein) as “classical” GCD models and refer to models in this paper as “pulsationally-assisted” GCD models or simply “pulsational” GCD models. The origin of the name stems from the fact that the white dwarfs in the models

in this paper undergo a pulsation where they first expand due to energy input from the deflagration phase and then contract due to the pull of gravity. These models require the contraction of the white dwarf to create the thermodynamic conditions necessary to initiate a detonation, hence the phrase “pulsationally-assisted”. In fact, the paradigm we put forth has characteristics of both the classical GCD models and the PRD models.

In section 2 of this paper we discuss the Zel’dovich gradient mechanism as a detonation trigger and its implications for the pulsational GCD. We give an overview of the FLASH code and the relevant physics modules used for our SNe Ia simulations in section 3. In section 4 we describe the evolution of our simulations. We compare the detonation mechanisms between the classical GCD and the pulsational GCD models in section 5. Finally, in section 6 we discuss properties of the simulations as well as possible observational features of the models.

2. Detonation Mechanism

In the pulsationally assisted version of the GCD model, a plume of hot ash plunges into the star during its contraction phase and initiates a detonation. Initially, as the plume advances around the star, a mixing layer of cold fuel and hot ash is formed at the plume-star interface. Compression due to the stellar contraction and to the plume pushing to higher density layers of the star, acts to heat the mixture. In the mixing layer the composition transitions from pure ash in the plume to pure fuel in the star, resulting in a compositional and temperature gradient in the mixing layer. A spontaneous detonation is triggered by the Zel’dovich gradient mechanism (Zel’dovich et al. 1970) when the mixture reaches the critical conditions.

The Zel’dovich mechanism requires an induction time gradient resulting from gradients

in both temperature and/or in composition. Rapid combustion in the high temperature region results in a shock wave as the burning front progresses to regions of low temperature. If the gradients are shallow enough and the combustion becomes associated with the shock, a detonation is formed; otherwise, the shock wave runs ahead of the burning front and the plasma does not detonate.

Much work has been done to determine the properties of the gradients required to successfully initiate a detonation by the Zel’dovich gradient mechanism (Arnett & Livne 1994; Niemeyer & Woosley 1997; Khokhlov et al. 1997; Röpke et al. 2007b; Seitenzahl et al. 2009b). Both Röpke et al. (2007b) and Seitenzahl et al. (2009b) studied systems initialized with constant density, constant composition, and a temperature gradient. Röpke et al. (2007b) examined the results of a linear temperature gradient. Seitenzahl et al. (2009b) performed a more comprehensive study with several functional forms for the temperature gradient and a wider range of conditions. The goal of the work was to determine the minimum size of the region containing the induction gradient for a self sustaining shock-reaction complex to form. This minimum size (or critical length scale, L_c) was determined to be a function of the input parameters of the system — the ambient temperature, ambient density, peak temperature, and steepness of the temperature profile. In summary, they find that for densities greater than or equal to 1×10^7 g/cm³ and for peak temperatures greater than 2×10^9 K, a conservative estimate of the critical length scale is $L_c \lesssim 10$ km.

Khokhlov et al. (1997) examined the conditions under which the Zel’dovich gradient mechanism would produce a detonation given a gradient in both temperature and composition. They study two cases: In the first case turbulence tears apart an active flame and mixes cold fuel with hot ash to achieve the necessary conditions to initiate a detonation. In the second case, stellar expansion extinguishes the active flame allowing the hot ash and cold fuel to mix. As the star contracts, it squeezes the mixture - creating the

necessary conditions for the mixture to detonate.

Khokhlov et al. (1997) argue that mixing is important in order for fuel to attain a high enough temperature to ignite at relatively low densities. They point out that cold fuel that obeys a white dwarf equation of state would have to be compressed to $\approx 1 \times 10^{10}$ g/cm³ in order to ignite; however, mixing hot ash at a level as low as 10% raises the entropy enough that the mixture would ignite at densities $\approx 10^7$ g/cm³. Their Figure 2 shows the critical density for ignition as a function of fuel mass fraction in the mixture.

In Khokhlov et al. (1997), a temperature gradient is set up in the mixing layer between cold fuel and hot ash. The temperature of the mixture is low in regions dominated by fuel and is high in regions dominated by ash. It is thus a matter of compressing the mixture to the critical density (and thus the critical peak temperature through compressional heating) for a detonation to initiate in the mixture. Their Figure 6 shows L_c as a function of critical density for a gas initialized with a linear compositional gradient and an temperature gradient determined by the amount of ash in the mixture at a particular location. They conclude that in the white dwarf environment, a detonation is possible for densities between 5×10^6 g/cm³ and $2 - 5 \times 10^7$ g/cm³. For a mixture density $\approx 1 \times 10^7$ g/cm³ the critical length is on the order of 10 km which is commensurate with the results of Seitenzahl et al. (2009b) even though the two approaches were distinct.

For the purposes of the following analysis, we take the critical density, $\rho_c = 1 \times 10^7$ g/cm³ and the critical length scale $L_c = 10$ km as the nominal values required for detonation.

The pulsationally assisted GCD detonates in the same manner as the second case described in Khokhlov et al. (1997). Here, ash ejected from the star flows over the surface to the collision region. As the ash flows, it turbulently mixes with fuel on the surface forming a mixing layer of fuel and ash. The growth of Kelvin-Helmholtz instabilities drives

the turbulent mixing. Using typical values from the conditions present at the surface-ash interface, we can approximate the largest unstable length scale, λ_{max} , such that all $\lambda \leq \lambda_{max}$ would grow due to the instability. Using linear stability analysis, the largest unstable length scale is expressed in terms of the physical conditions at the interface between the flowing ash and the surface of the white dwarf as

$$\lambda_{max} = \frac{2\pi \cdot \alpha_{fuel} \alpha_{ash} U^2}{g(\alpha_{fuel} - \alpha_{ash})}, \quad (1)$$

where $\alpha_{fuel} = \frac{\rho_{fuel}}{\rho_{fuel} + \rho_{ash}}$, $\alpha_{ash} = \frac{\rho_{ash}}{\rho_{fuel} + \rho_{ash}}$, ρ_{fuel} is the fuel density (i.e. the surface density of the white dwarf), ρ_{ash} is the ash density, $g \approx 1 \times 10^9$ cm/s² is the acceleration due to gravity, and U is the velocity of the ash (Chandrasekhar 1961). The ash flows at a speed $U \approx 5 \times 10^8$ cm/s and the interface is located at $r_{interface} \approx 5 \times 10^8$ cm from the center of the star. Values for the densities are $\rho_{fuel} \approx 1 \times 10^6$ g/cm³ and $\rho_{ash} \approx 1 \times 10^5$ g/cm³. Inserting these values into Eq. (1) gives $\lambda_{max} \approx 1.0 \times 10^8$ cm - comparable to the radius of the star and hence $\gg L_c$. Therefore a region the size of L_c would develop Kelvin-Helmholtz instabilities which would drive turbulent mixing.

The ash must flow approximately half way around the star to reach the collision region. Using the values of U and $r_{interface}$ we can approximate the time it would take for the ash to reach the collision region, τ_{ash} , as

$$\tau_{ash} = \frac{\pi \cdot r_{interface}}{U} \quad (2)$$

Therefore $\tau_{ash} \approx 1$ s. The timescale for the growth of the unstable Kelvin-Helmholtz modes with length scale λ (Chandrasekhar 1961) in the linear regime is

$$\tau_{KH}(\lambda) = [g(2\pi/\lambda)(\alpha_{fuel} - \alpha_{ash}) - (2\pi/\lambda)^2 \alpha_{fuel} \alpha_{ash} U^2]^{-1/2}. \quad (3)$$

The growth time scale for a perturbation of length scale $\lambda = L_c$ km is $\tau_{KH}(10km) \approx 1 \times 10^{-3}$ s. Since $\tau_{ash} \gg \tau_{KH}(10km)$, perturbations of length scale L_c will grow for several (linear

analysis) e-folding times before the ash reaches the collision region. Therefore, the flows have ample opportunity to create a mixing layer of fuel and ash of the size of the critical length scale required for a detonation in the time it takes for the ash to reach the collision region.

We conclude that the Zel’dovich mechanism can trigger a detonation in the mixed fuel-ash layer. The ash flows turbulently mix with fuel on the surface driven by Kelvin-Helmholtz instabilities. The mixing process produces the necessary thermal and compositional gradients and the increase in density of the mixture as it pushes into the star both accelerates the combustion and lowers the critical length scale, L_c , required for the gradients. Thus, the pulsationally assisted GCD model is a viable mechanism to trigger a detonation.

3. Numerical Methods

We use the Adaptive Mesh Refinement (AMR) FLASH application framework (Fryxell et al. 2000; Dubey et al. 2009) to perform the simulations presented in this paper. FLASH is a modular, component-based application code framework created to simulate compressible, reactive astrophysical flows. The framework supports multiple methods for managing the discretized simulation mesh, including the PARAMESH (Parallel Adaptive Mesh Refinement) library (MacNeice et al. 2000), which implements a block-structured adaptive grid.

FLASH includes a directionally split piecewise-parabolic method (PPM) solver (Colella & Woodward 1984) descended from the PROMETHEUS code (Arnett et al. 1989). It has been successfully applied to a wide variety of large-scale terrestrial and astrophysical flow problems, ranging from simulations of homogeneous, isotropic turbulence (Benzi et al.

2008; Arnèodo et al. 2008), Raleigh-Taylor instability (Calder et al. 2002), shock-cylinder interaction (Weirs et al. 2005), and laser-driven high energy density laboratory experiments (Kane et al. 2001), to buoyancy-driven turbulent combustion (Townesley et al. 2008), wind-driven instabilities in neutron star atmospheres (Alexakis et al. 2004), contact binary stellar evolution (Ricker & Taam 2008), Type Ia supernovae (Jordan et al. 2008; Meakin et al. 2009; Jordan et al. 2009), galaxy collisions (ZuHone et al. 2008), and cosmological simulations of large-scale structure formation (Heitmann et al. 2005).

The energetics scheme used to treat flames and detonation waves in our simulations uses three progress variables to track carbon burning, QSE relaxation, and NSE relaxation. Details concerning the nuclear physics and the numerical implementation are presented in Calder et al. (2007); Townesley et al. (2007); Seitenzahl et al. (2009c). Subsonic burning fronts (deflagrations) are advanced using an advection-diffusion-reaction (ADR) equation. Details concerning the implementation, calibration and noise properties of the flame treatment can be found in Townesley et al. (2007) and references therein. Detonations are handled naturally by the reactive hydrodynamics solver in FLASH without the need for a front tracker. This approach is possible because unresolved Chapman-Jouguet (CJ) detonations retain the correct jump conditions and propagation speeds. Cellular structure smaller than the grid scale will be suppressed in our simulations but is free to form on resolved scales. The impact of cellular structure on the global evolution of the model is still uncertain; however, since cellular structure alters the detonation wave speed by only a few percent for the conditions being modeled (Timmes et al. 2000), the effect is likely to be small. Additional details related to the treatment of detonation waves are discussed in Meakin et al. (2009).

Self gravity is calculated by expanding the mass density field in multipole moments, which are used to approximate the scalar gravitational potential. The gravitational

acceleration is calculated by approximating the derivative of the scalar potential at each location in the domain. The Helmholtz equation of state of Timmes & Swesty (2000) is used to describe the thermodynamic properties of the stellar plasma, including contributions from blackbody radiation, ions, and electrons of an arbitrary degree of degeneracy.

4. Simulations and Results

We extended the study of the GCD model described in J08 with two primary differences. First, we included detonation physics in the simulations and followed the models from ignition, through the detonation phase, and to the free expansion phase. We terminated the simulations when the temperature decreases to the point that nuclear reactions ceased. Second, we initiated these simulations with multiple ignition points (as described in Jordan et al. (2009)) instead of a single ignition point.

4.1. Simulation Setup

We initialized the simulations identically to those found in J08 except that we used more than one ignition point. For completeness we give the basic points here but refer the reader to J08 and references therein for more details.

Our simulations used FLASH’s AMR capabilities with a finest resolution of 8km. Each simulation contained a $1.365 M_{\odot}$ white dwarf in hydrostatic equilibrium composed of equal parts carbon and oxygen. The white dwarf had a central density of 2.2×10^9 g/cm³, an ambient temperature of 3×10^7 K, and a radius of approximately 2000 km. Although the core of the star is most likely convective with a turbulent convective RMS velocity $v_{\text{RMS}} \sim 16$ km/s (Nonaka et al. 2012), the turbulent convective RMS velocity is much less than the laminar flame speed, and so we have ignored the background convective

turbulence, and initialized the star with zero velocity.

We initiated this series of simulations with multiple ignition “points”, 16 km spheres comprised of hot ash placed in the star at rest. We placed the ignition points in a spherical region whose center coincided with the z-axis. We parameterized the spherical region by its radius and z-offset (the distance from the origin of the center of the spherical region along the z-axis). The radius of the spherical region was 128 km and the z-offsets were 68 km, 88 km, and 168 km - one z-offset for each of our three simulations. We randomly populated a 128 km spherical region with 63 ignition points. We placed ignition points so that they did not overlap with one another, and so that they were contained entirely within the spherical region. We used the same random distribution of ignition points for all three simulations; they only differed by their relative location along the z-axis. Table 1 contains labels for the simulations referred to in this work along with parameters for the initial conditions.

These initial conditions serve to represent two physical situations that may occur in the white dwarf. First, it may be possible that ignition occurs at multiple points. Recent work by Zingale et al. (2011) and Nonaka et al. (2012) of the last moments of the smoldering phase before ignition conclude that a single ignition point is the most probable scenario; however, ignition is an inherently stochastic process and many realizations are required to make definitive statements about all of the possible outcomes. Currently only a handful of simulations exist. Furthermore, the process of forming hot spots in the simulations that eventually lead to an ignition may be resolution dependent as stated in Nonaka et al. (2012), and leaves open the door for a multiple ignition point scenario. Finally, all but one of the simulations in Zingale et al. (2011) and Nonaka et al. (2012) were stopped once a hot spot formed that lead to ignition. Therefore, it may have been possible for more ignition points to form after the initial runaway, even though in the specific simulation that they continued past the formation of initial ignition point no secondary ignition points were

observed (Nonaka et al. 2012).

Second, though we ignore the convective turbulence, most likely convective plumes exist with a velocity ~ 100 km/s (Nonaka et al. 2012). This is comparable to the flame speed and can potentially grow the flame surface through the Kelvin-Helmholtz instability. We essentially mock-up this effect by initializing our simulations with multiple ignition points in close proximity to one another. These ignition points in turn quickly merge and form a single asymmetric burning region enclosed by a distorted flame surface.

4.2. Simulation Narrative

In this section we describe the evolution of the pulsational GCD model. Figures 1 and 2 show snapshots of the $63n128r168z$ simulation starting with the initial conditions and ending with the passage of the detonation wave. The green contour in the figures approximates the location of the surface of the white dwarf. The orange regions are high temperature regions. These regions are primarily hot ash. The temperature ranges from 1×10^9 K (dark orange) to 5×10^9 K (bright orange).

Each simulation begins with one of the above multiple ignition point configurations. Panel (a) of Figure 1 shows the initial conditions of the $63n128r168z$ simulation. In the first few tenths of a second, each ignition point quickly burns radially outward from its center and merges with the other ignition points to form a large asymmetric bubble of ash. The ash in the bubble is less dense than the surrounding stellar material and is therefore buoyant. After 0.3-0.4 seconds, the bubble, which continues to grow in size, begins to quickly rise towards the surface of the white dwarf. During the rise, Rayleigh-Taylor instabilities grow on the flame surface, which further increases the complexity of the surface and enhances the burning rate (Khokhlov 1995; Townsley et al. 2008).

Panel (b) of Figure 1 shows the simulation at 0.6s. This panel shows the ignition points after they have risen and merged to form a complex volume whose surface has been enhanced by fluid instabilities.

After approximately 1.5 s the rising ash bubble breaks through the stellar surface and begins spreading laterally across the star in all directions, converging on a region antipodal to the bubble breakout region. Since the density of the surface layers of the star are too low to maintain thermonuclear combustion, the flame quenches and the deflagration subsides. As the ash flows over the surface of the star, cold fuel (C and O) mixes with the ash at the interface between the ash and the stellar surface, creating a fuel-ash mixture.

Panels (c), (d), and (e) of Figure 1 are at 1.1 s, 1.4 s, and 1.9 s, respectively. These panels show the ash after it has broken out of the surface and has started to spread. In panel (c) the ash has spread approximately half way around the star. By 1.4 s (panel d), the ash has made it three-fourths the way around the star. At 1.9 s (panel e), the ash has almost completely engulfed the white dwarf.

A significant amount of nuclear energy, ranging from 1.9×10^{50} to 3.9×10^{51} erg (comparable to the binding energy of the white dwarf) is released during the deflagration. This provides a kick to the star which causes it to undergo a large amplitude pulsation. During the first few seconds, while the ash flows over the surface, the star expands to several times its original size. The expanding star slows the ash before it reaches the collision region. This shown in panels (c) - (f) of Figure 1 and panel (a) of Figure 2. Panel (f) of Figure 1 is at 2.2 s and panel (a) of Figure 2 is at 2.5 s. These two panels show the star as it is expands. The ash seems to disappear from the panels because the star has expanded and the ash has cooled to the point that it has fallen out of the color range. Panel (b) of Figure 2 is at 3.1 s. The white dwarf is maximally expanded in this image.

Several seconds after the ash is ejected from the surface of the star, it converges at the

opposite pole from where it broke out. The converging flow compresses the material in the collision region until the pressure is sufficient to stop the mixture from flowing laterally and to drive a plume of fuel and ash towards the interior of the star. Additionally, after the star has reached its maximum pulsational amplitude, it begins to contract. This contraction increases the global density structure of the star, and thus the local density of at the collision region, eventually resulting in explosive C and O burning, as detailed in section 2. The combustion immediately transitions into a detonation that sweeps across the star in a few tenths of a second.

Panels (c) and (d) of Figure 2 (at 3.7 s and 4.2 s respectively) show the star as it contracts. A hot region can be seen forming at the “bottom” of the star. This hot region is the result of the compressional heating of the mixture in the collision region from the work done by the contracting star as well as the material flows themselves. Panel (e) of Figure 2 is at 4.3 s and shows the simulation just after the initiation of the detonation wave. Panel (f) of Figure 2 shows the simulation at 4.4 s. The detonation wave has consumed about half of the star in just over 0.1 s.

The detonation wave transforms the white dwarf into a super-heated remnant composed of NSE material in the core surrounded by a layer of intermediate mass elements and topped off with the ash of partially burned C and O. This whole structure is shrouded by the products of the deflagration which consisted of NSE material, intermediate mass elements, carbon burning products, and unburned C and O. The super-heated structure quickly expands and cools, and is transitioning into a homologous structure when the simulations are stopped.

4.3. Simulation Details

The main properties of the three simulations are summarized in Table 1. The simulations differ in the location of the center of their sphere of ignition points, and are labeled *63n128r68z* (ignition sphere centered 68 km from the center of the star), *63n128r88z* (88 km from the center of the star), and *gcdsim168* (168 km from the center of the star).

The deflagration phase of the SN Ia provides a kick to the white dwarf which causes the white dwarf to rapidly expand and then contract. It is the expansion and subsequent detonation on contraction that characterizes the pulsation GCD model. Figure 3 shows the amount of nuclear energy release as a fraction of the binding energy of the star as a function of time for the three simulations. The simulations trended together for the first 0.8s and then diverged. The deflagration continued to release nuclear energy until approximately 1.5s in each simulation, at which time the flame stopped burning. In general, the simulations whose ignition points were placed closer to the core of the white dwarf burned more during the deflagration and thus imparted more energy to the star. Simulation *63n128r168z* had its configuration of ignition points placed farthest from the core of the star and thus burned the least where as the *63n128r68z* had its ignition points placed closest to the core of the star and thus the deflagration phase released the most nuclear energy during this simulation. The amount of energy released ranged from 18.9×10^{49} erg to 38.6×10^{49} erg, or between 38% and 78% of the binding energy of the star. By comparison, the single bubble initial conditions in J08 released between 3.0×10^{49} erg and 10.5×10^{49} erg, or between 6% and 21% of the binding energy of the white dwarf.

The energy released during the deflagration phase was sufficient to cause the star to undergo an energetic pulsation. Figure 4 shows the evolution of the central density of the white dwarf for the three simulations and gives a measure of the strength and the period of the pulsation. In each simulation, the white dwarf expanded to a maximum

amplitude and then contracted before detonating. The simulation that expanded the least was *63n128r168z* which reached a minimum central density, $\rho_{c,min}$, of 3.51×10^7 g/cm³. The star expanded for 3.1 s before it began to contract. By contrast, *63n128r68z* achieved $\rho_{c,min} = 0.43 \times 10^7$ g/cm³, and the white dwarf did not begin to contract until 4.71 s. Thus the simulation in which the most energy was released during the deflagration phase - *63n128r68z* - experienced the most expansion and had the longest pulsational period. Simulation *63n128r168z*, in which the least energy was released, expanded least, and had the shortest pulsational period. The *63n128r88z* simulation released an intermediate amount of energy compared to the other two simulations and has intermediate values of $\rho_{c,min}$ and the pulsation period. The vertical lines in Figure 4 mark the time at which the star detonates.

As the white dwarf expanded, ash was ejected from the surface and flowed laterally over the star, mixing with surface fuel as it flowed. Figure 5 plots the polar angle of the leading edge of the flow as a function of time. Initially a small region of ash crossed the origin and was responsible for the large values of θ seen in the figure during the first second. After one second, the ash reached the surface and started to spread around the star. For each simulation, the ash (fuel-ash mixture) quickly reached a polar angle of approximately 150° and then stalled. This was in part because the mixture pushed some material in front of it which compressed material in the collision region and increased the pressure there. Also, the expansion of the star robbed kinetic energy from the flow which also contributed to the mixture stalling. Once the star contracted, the mixture slowly pushed its way further around the star, as well as into the high density regions towards the core. As before, the lines on the graph highlight the time at which the star detonated. For the *63n128r168z* simulation whose white dwarf had the shortest pulsational period, the mixture stalled for a short period of time. The *63n128r68z* simulation’s white dwarf had the longest pulsational period, and therefore the fuel-ash mixture was stalled in the collision region for longer.

Even though the mixture encroached on the collision region within a few seconds from when the flow started, it was the contraction of the star that assisted the mixture in making the final move to higher densities.

After the star began to contract, the fuel-ash mixture made its way into the high-density layers of the white dwarf. Figure 6 shows the evolution of the thermodynamic conditions in the fuel-ash mixture as it pushed into the star. The top plot in Figure 6 shows the temperature of the computational cell with the maximum temperature in the mixture. The middle plot shows the density in the cell with the maximum temperature as described above. The bottom plot shows the radius of the that computational cell. Both the temperature and density follow the trend of the central density, as the white dwarf expanded and contracted. As the star expanded, the temperature and density of the mixture decreased. As the star contracted, the temperature and density of the mixture increased. The location of the hot spot followed the same pattern; hence, as the star contracted, the radius of the hot spot moves closer to the core. This was due both to the stellar contraction and the continued flow of the mixture. Once the temperature of the hot spot exceeded $\sim 1.5 \times 10^9$ K and the density exceeded $\sim 2 \times 10^7$ g/cm³ rapid combustion ensued in the mixture, which quickly transitioned into a detonation. The *63n128r168z* simulation detonated earliest and the *63n128r68z* simulation detonated latest. The *63n128r168z* simulation expanded least and thus its contraction happened sooner, which in term transitioned the conditions in the fuel-ash mixture to those that would trigger a detonation earlier. The *63n128r68z* simulation expanded for a longer period of time, decompressed to a greater degree and thus it took longer for the star to begin to contract, and, when it did, it had to increase the stellar density by a higher factor before detonation conditions could be reached.

Additionally, the simulations showed that the detonation location has a higher radius for the simulation that burned the most during the deflagration and has the smallest

radius for the simulation the burned the least. The simulation that burned an intermediate amount during the deflagration has an intermediate value of the radius of the detonation location.

An important set of observables of an SN Ia are the nucleosynthetic yields produced in the event. We have approximated the yields from the three models using the reaction progress variables from FLASH’s burning module (Calder et al. 2007). Table 2 lists the post-explosion nucleosynthetic yields in terms of the quasi-static equilibrium groups that are represented by the progress variables for the three simulations. Note that the material that burned to nuclear statistical equilibrium (NSE) is predominately ^{56}Ni . The ^{56}Ni produced during these simulations ranges from ~ 1.0 to $\sim 0.7 M_{\odot}$. Though yields of $\sim 1.0 M_{\odot}$ of ^{56}Ni are associated with luminous SNe Ia, yields of $\sim 0.7 M_{\odot}$ of ^{56}Ni are associated with SNe Ia of normal luminosity. The combined mass of the intermediate mass elements and NSE material is $1.1 M_{\odot}$ and is consistent with observed SNe Ia (Mazzali et al. 2007).

The deflagration phase of the pulsational GCD models burns approximately 0.1 - 0.25 M_{\odot} of material. This material is ejected into the outer regions of the system, surrounding the white dwarf when it detonates. Table 3 lists the nucleosynthetic yields produced during the deflagration phase of the three simulations. The primary product of the deflagration phase is NSE material with about a third of the material composed of carbon burning products and intermediate mass elements.

These simulations show that through the course of an off-centered ignition, if a detonation is not triggered as the flame breaks down as it moves through the low density layers of the star on its way to the surface (i.e. the first scenario in (Khokhlov et al. 1997)) and if the energy release during the deflagration is sufficient to significantly disrupt the star and cause it undergo a large amplitude pulsation, ash will flow around the surface (mixing with cold fuel as it flows), and stall in the collision region while the star is expanding.

As the white dwarf contracts, the conditions in the fuel-ash mixture are pushed to higher temperature and density until the values exceed that required for detonation, at which time a detonation is triggered in the mixture and consumes the star.

5. Comparison of Detonation Mechanism to Previous GCD Models

The classical GCD model of SNe Ia is postulated to be possible if the energy released during the deflagration phase does not significantly expand the star. With little stellar expansion, the fuel density in the collision region is high enough for compression by the inflowing ash to increase the temperature in the fuel and ultimately initiate a detonation. Figure 7 shows the evolution of the classical GCD model (16b100o8r from J08) leading up to the detonation. The top left panel of the figure is at $t=1.8$ s. It shows the ash as it approached the collision region. Fuel pushed ahead of the ash increased in temperature due to compressional heating. This hot region formed a jet that flowed both towards and away from the surface of the star. The top right panel is at $t=1.9$ s. The ash converged further into the collision region. The hot fuel continued to increase in temperature and had begun to slowly burn carbon as a result. This smoldering also increased the fuel temperature. The bottom left panel is at $t=2.22$ s. At this time the ash flows have collided. The hot fuel has further increased in temperature due to further compressional heating and due to combustion. The head of the hot jet has pushed the high temperature region and has reached the higher density layers of the white dwarf. The thermodynamic conditions appropriate for a detonation have been met and the hot smoldering material launched a detonation. The formation of the detonation can be seen at the head of the hot jet. Finally, the bottom right panel at $t=2.3$ s shows the simulation after the detonation occurred. The detonation wave is propagating outward from its initiation point. The high temperature region behind the detonation as well as the smooth detonation front is visible in this image.

The pulsational GCD model of SNe Ia is possible if the deflagration phase releases enough energy to cause the white dwarf to expand significantly and then contract but not so much energy that the star becomes unbound. Figure 8 shows the evolution of the pulsational GCD model, *63n128r168z*, leading up to the detonation. The top left panel is at $t=3.5$ s where the mixture was beginning to approach the collision region. In contrast to the classical GCD, the ash flows and collision region were at low densities and no compressional heating of the fuel in the collision region occurred. The top right panel is at $t=3.8$ s. Note that this panel is zoomed with respect to the previous panel. The fuel-ash mixture continued to push into the collision region. The mixture began to heat since the white dwarf was contracting and the ash was pushing to higher densities in the direction towards the core of the white dwarf. The bottom left panel is at $t=4.1$ s. Note that this panel is zoomed in from the previous panel. The white dwarf has continued to contract and the mixture continued to move to higher densities. The mixture heated significantly due to 1) compressional heating due to the fact that the mixture pushed to higher densities and that the star was in the process of contracting and 2) the mixture reached conditions that caused it to smolder. The mixture then approached the critical density above which a detonation would be initiated. The bottom left panel is at 4.22s Note that this panel is zoomed in from the previous panel. The mixture reached the critical temperature and density and a detonation was triggered as described in section 2. Two detonation waves can be seen emerging from the mixture layer in the image. The bottom right panel is at $t=4.3$ s. The detonation is propagating outward from its initiation point through the star. The high temperature region behind the detonation wave as well as the smooth detonation front are clearly visible.

In summary, the classical GCD model detonates as the white dwarf is expanding. The thermodynamic conditions for detonation are reached when the ash flows compress and heat fuel in the collision region and force this hot fuel into the high density layers of

the star. In contrast, the pulsational GCD model detonates as the white dwarf contracts. The thermodynamic conditions for detonation are achieved by the combination of the contraction of the white dwarf which increases the temperature and density of the fuel-ash mixture, as the mixture pushes its way towards the high density core of the white dwarf.

6. Discussion

6.1. Caveats

We would first like call the reader’s attention to several numerical issues related to the simulations. First, the initiation of the detonation is unresolved. In section 2 we point out that the critical length scale in of the mixture is on the order of 1 - 10 km. Since the best spatial resolution of the simulation is 8 km, the initiation of the detonation is severely under-resolved. Numerically, the detonation occurs because a computational cell contains enough fuel and has achieved a high enough temperature and density that the carbon burning reaction rate is extremely high. All of the fuel in the cell burns in a single computational time step. This releases a tremendous amount of energy in the cell, which dramatically increases the temperature and pressure in the cell, and creates a shock with the neighboring cells. The shock propagates outwards from the cell and burns material in its wake, forming a detonation. Since the initiation of the detonation is purely numerical in nature, we stress that it simply indicates that a computational cell has reached the appropriate thermodynamic conditions and fuel-ash ratio and nothing more. We refer the reader to Meakin et al. (2009) and Seitenzahl et al. (2009b,a) for a discussion the initiation of detonations in the context of numerical simulations.

Second, in our description of the detonation mechanism, we appeal to the fact that the ash ejected from the white dwarf will mix with fuel on the surface of the star as it

flows; however, we do not treat mixing on unresolved scales. Mixing on small scales occurs by numerical diffusion. Though we do not capture the details of that mixing process, we nevertheless fully expect the material to be well mixed as it flows around the star as postulated in section 2.

6.2. Properties of the Pulsational GCD Models

6.2.1. *Robustness of Detonation Mechanism*

In the classical GCD model, flowing ash must compress fuel in the collision region to achieve the thermodynamic conditions necessary to launch a detonation. This would seem to require the ash flows to converge symmetrically in the collision region so that they focus on a localized region. Thus far, the only successful classical GCD simulations have been performed in 2D cylindrical geometry ((Meakin et al. 2009) for example) which imposes azimuthal symmetry, and in 3D with single bubble ignition points as initial conditions which, by their nature, evolve in an azimuthally symmetric manner. Our pulsational GCD models were initiated with multiple ignition points. These ignition points evolved into an asymmetric volume of ash which produced asymmetric ash flows on the surface. However, the pulsational GCD depends less stringently on the details of the ash flows. As long as the mixture is redirected towards the core of the star, the contraction of the white dwarf will do the rest, even if the flow lacks symmetry. As a result, the pulsational GCD model, in principle, contains a robust detonation mechanism that only depends on getting the fuel-ash mixture to a high enough density as the star contracts.

6.2.2. *Nucleosynthesis*

For any SN Ia model, the luminosity of the model is strongly related to the amount of ^{56}Ni produced in the explosion. This depends in turn on the density of the plasma before it is burned. A fair rule of thumb is that if $\rho \gtrsim 1.0 \times 10^7 \text{ g/cm}^3$ then that material will burn to NSE, which is predominantly ^{56}Ni (see e.g., the comparison made in figure 12 of Meakin et al. (2009) and the discussion in their Section 5). The white dwarf in the pulsational GCD model is contracting from an expanded state when it detonates. As a result, there is a reduced amount of high density material and thus it is in principle possible for the model to produce range of abundances of ^{56}Ni - and thus of luminosities - depending on the expanded state of the white dwarf when it detonates. The classical GCD models described in J08 detonate as the white dwarf is expanding after a weak deflagration phase. The star is still fairly compact and there is ample high density material when the star detonates. The amount of ^{56}Ni produced in each of those models is greater than $1 M_{\odot}$ which corresponds to overly luminous SNe Ia. By contrast, the pulsational GCD model is more easily able to access regions in model space that correspond to standard values of ^{56}Ni production.

6.2.3. *Observational Features of the Pulsational GCD Model*

The pulsational GCD model has a post detonation geometry similar to the classical GCD model. The explosion is the result of a single off-centered detonation. The location of the detonation is at the antipodal point from where the star ejected the ash from its interior. This confers approximate azimuthal symmetry upon the system.

In the pulsation GCD model, the star detonates after the cessation of the deflagration phase. There is no active flame in the interior of the star at the time of detonation and

thus no compositional inhomogeneities from deflagration ash. When the detonation occurs, it produces a smooth interior of NSE material surrounded by a layer of intermediate mass elements. The intermediate mass elements would then be surrounded by a shroud of the ash produced in the deflagration. The flow of this ash over the surface of the white dwarf produces a clumpy, choppy outer boundary to the intermediate mass element layer of the remnant. This is similar to structure suggested by the spectropolarimetry measurements of Wang et al. (2006, 2007). Furthermore, very early spectra taken at ~ 1 day after the explosion from the SN Ia 2011fe show that there is O, Mg, Si, S, Ca, and Fe - which are products of the deflagration in our models - in the outer most layers of the remnant (Nugent et al. 2011). Finally, table 1 lists the post explosion kinetic energy for the three simulations. These energies are $\sim 1 \times 10^{51}$ ergs and are consistent with observations of SNe Ia.

6.3. Comparison to Previous Work

It is interesting to compare our results to the results from the 3D simulations in Röpke et al. (2007b). They initialize their simulations with a single spherical bubble, a region of small bubbles emulating a single bubble with surface perturbations, and a configuration of bubbles confined to a tear-drop-shaped envelope. Of the six 3D simulations they performed, two of the white dwarfs in the simulation became unbound due to the energy released during the deflagration phase. Of the four simulations in which the white dwarf remained bound, the deflagration energy release was in the range of $1 \times 10^{50} - 3.3 \times 10^{50}$ erg, or roughly $\sim 20\% - 60\%$ of the binding energy of the white dwarf. Furthermore, one of their single-bubble ignition model released 2.79×10^{50} erg — comparable to our 63n128r88z simulation (their other single bubble ignition model disrupted the star). These values of the energy released during the deflagration phase are similar to those presented in our work.

They found that the conditions for detonation are not reached in any of their simulations; however, they stopped their simulations when the conditions for detonation are not met in the scenario presented in J08. Had they continued their simulations and allowed the star to contract, there is a good chance that they would have found the conditions that we have discovered here – a possibility alluded to in their conclusion.

7. Conclusion

We have conducted a series of numerical experiments simulating the evolution of a white dwarf star in which we initiate a deflagration at off-center ignition points. The amount of energy released during the deflagration phase is enough to cause the star to undergo an energetic pulsation. As in the classical GCD model, the off-center ignition leads to a plume of material that is ejected from the star, flows laterally over the stellar surface, and converges on a collision region at the antipodal point from the ash breakout point. As the white dwarf contracts, it creates thermodynamic conditions of material in the collision region appropriate for the Zel’dovich gradient mechanism to launch a detonation. We find that the conditions for detonation are reached in all three of our models. The energy deposition from the deflagration phase in these models ranges from 38% to 78% of the binding energy of the white dwarf. We further comment that the detonation mechanism in the pulsational GCD depends only on the bulk fluid motion of the system after the deflagration is ignited as opposed to a specific flow pattern, such as the focusing of the ash flows in the collision region in the classical GCD. This property confers a measure of robustness to the detonation mechanism.

Finally, the features of the pulsational GCD qualitatively agree with the observations of SNe Ia, insofar as such comparisons can be made without subjecting the remnant to a radiation transfer treatment in order to compute actual light curves. The three models

produced yields of ^{56}Ni ranging from $0.72 M_{\odot}$ to $0.98 M_{\odot}$. These ^{56}Ni yields are less than those produced in the classical GCD models of J08, primarily because the white dwarf in our models is in a more expanded state at the time of detonation and contains a lower abundance of high-density, NSE-producing matter. This class of models allows SNe Ia to evolve and detonate with characteristics similar to the classical GCD while producing supernovae of lower luminosity.

The authors thank the FLASH Code Group, especially Chris Daley and Anshu Dubey for help with the development of and troubleshooting the code. We thank Brad Gallagher for creating figures 1 and 2. We also thank Katherine Riley, Mike Papka, and the staff at the Argonne Leadership Computing Facility at Argonne National Laboratory for help running our large-scale simulations on Intrepid at ANL. This work was supported in part at the University of Chicago by the U.S Department of Energy (DOE) under Contract B523820 to the ASC Alliances Center for Astrophysical Nuclear Flashes, and in part by the National Science Foundation under Grant No. AST - 0909132 for the “Petascale Computing of Thermonuclear Supernova Explosions”. This research used computational resources awarded under the INCITE program at ALCF at ANL, which is supported by the Office of Science of the US Department of Energy under Contract No. DE-AC02-06CH11357.

We dedicate this work to the memory of our colleague and dear friend, Nathan Hearn.

REFERENCES

- Alexakis, A., Calder, A. C., Heger, A., Brown, E. F., Dursi, L. J., Truran, J. W., Rosner, R., Lamb, D. Q., Timmes, F. X., Fryxell, B., Zingale, M., Ricker, P. M., & Olson, K. 2004, *ApJ*, 602, 931
- Arnèodo, A., Benzi, R., Berg, J., Biferale, L., Bodenschatz, E., Busse, A., Calzavarini, E., Castaing, B., Cencini, M., Chevillard, L., Fisher, R. T., Grauer, R., Homann, H., Lamb, D., Lanotte, A. S., Lévêque, E., Lüthi, B., Mann, J., Mordant, N., Müller, W., Ott, S., Ouellette, N. T., Pinton, J., Pope, S. B., Roux, S. G., Toschi, F., Xu, H., & Yeung, P. K. 2008, *Physical Review Letters*, 100, 254504
- Arnett, D., Fryxell, B., & Mueller, E. 1989, *ApJ*, 341, L63
- Arnett, D. & Livne, E. 1994, *ApJ*, 427, 330
- Benzi, R., Biferale, L., Fisher, R. T., Kadanoff, L. P., Lamb, D. Q., & Toschi, F. 2008, *Physical Review Letters*, 100, 234503
- Branch, D., Buta, R., Falk, S. W., McCall, M. L., Uomoto, A., Wheeler, J. C., Wills, B. J., & Sutherland, P. G. 1982, *ApJ*, 252, L61
- Bravo, E. & García-Senz, D. 2009, *ApJ*, 695, 1244
- Bravo, E., García-Senz, D., Cabezón, R. M., & Domínguez, I. 2009, *ApJ*, 695, 1257
- Calder, A. C., Fryxell, B., Plewa, T., Rosner, R., Dursi, L. J., Weirs, V. G., Dupont, T., Robey, H. F., Kane, J. O., Remington, B. A., Drake, R. P., Dimonte, G., Zingale, M., Timmes, F. X., Olson, K., Ricker, P., MacNeice, P., & Tufo, H. M. 2002, *ApJS*, 143, 201
- Calder, A. C., Townsley, D. M., Seitenzahl, I. R., Peng, F., Messer, O. E. B., Vladimirova, N., Brown, E. F., Truran, J. W., & Lamb, D. Q. 2007, *ApJ*, 656, 313

- Chandrasekhar, S. 1961, Hydrodynamic and hydromagnetic stability, ed. Chandrasekhar, S.
- Colella, P. & Woodward, P. R. 1984, *Journal of Computational Physics*, 54, 174
- Dark Energy Task Force. 2006, Report of the Dark Energy Task Force, Available online at
http://www.nsf.gov/mps/ast/aaac/dark_energy_task_force/report/detf_final_report.pdf
- Dubey, A., Antypas, K., Ganapathy, M., Reid, L., Riley, K., Sheeler, D., Siegel, A., & Weide, K. 2009, *Parallel Computing*, 35, 512
- Fryxell, B., Olson, K., Ricker, P., Timmes, F. X., Zingale, M., Lamb, D. Q., MacNeice, P., Rosner, R., Truran, J. W., & Tufo, H. 2000, *ApJS*, 131, 273
- Gamezo, V. N., Khokhlov, A. M., & Oran, E. S. 2004, *Physical Review Letters*, 92, 211102
- . 2005, *ApJ*, 623, 337
- Heitmann, K., Ricker, P. M., Warren, M. S., & Habib, S. 2005, *ApJS*, 160, 28
- Iben, Jr., I. & Tutukov, A. V. 1984, *ApJS*, 54, 335
- Jordan, G. C., Meakin, C. A., Hearn, N., Fisher, R. T., Townsley, D. M., Lamb, D. Q., & Truran, J. W. 2009, in *Astronomical Society of the Pacific Conference Series*, Vol. 406, *Astronomical Society of the Pacific Conference Series*, ed. N. V. Pogorelov, E. Audit, P. Colella, & G. P. Zank, 92–+
- Jordan, IV, G. C., Fisher, R. T., Townsley, D. M., Calder, A. C., Graziani, C., Asida, S., Lamb, D. Q., & Truran, J. W. 2008, *ApJ*, 681, 1448
- Kane, J. O., Robey, H. F., Remington, B. A., Drake, R. P., Knauer, J., Ryutov, D. D., Louis, H., Teyssier, R., Hurricane, O., Arnett, D., Rosner, R., & Calder, A. 2001, *Phys. Rev. E*, 63, 055401

Khokhlov, A. M. 1991, *A&A*, 245, 114

—. 1995, *ApJ*, 449, 695

Khokhlov, A. M., Oran, E. S., & Wheeler, J. C. 1997, *ApJ*, 478, 678

Kim, A., Linder, E., Miquel, R., & Mostek, N. 2004, *Monthly Notices of the Royal Astronomical Society*, 347, 909

MacNeice, P., Olson, K. M., Mobarry, C., de Fainchtein, R., & Packer, C. 2000, *Computer Physics Communications*, 126, 330

Maoz, D., Sharon, K., & Gal-Yam, A. 2010, *ApJ*, 722, 1879

Mazzali, P. A., Röpke, F. K., Benetti, S., & Hillebrandt, W. 2007, *Science*, 315, 825

Meakin, C. A., Seitenzahl, I., Townsley, D., Jordan, G. C., Truran, J., & Lamb, D. 2009, *ApJ*, 693, 1188

Niemeyer, J. C. & Woosley, S. E. 1997, *ApJ*, 475, 740

Nomoto, K. 1982, *ApJ*, 253, 798

Nomoto, K. & Kondo, Y. 1991, *ApJ*, 367, L19

Nomoto, K., Thielemann, F.-K., & Yokoi, K. 1984, *ApJ*, 286, 644

Nonaka, A., Aspden, A. J., Zingale, M., Almgren, A. S., Bell, J. B., & Woosley, S. E. 2012, *ApJ*, 745, 73

Nugent, P. E., Sullivan, M., Cenko, S. B., Thomas, R. C., Kasen, D., Howell, D. A., Bersier, D., Bloom, J. S., Kulkarni, S. R., Kandrashoff, M. T., Filippenko, A. V., Silverman, J. M., Marcy, G. W., Howard, A. W., Isaacson, H. T., Maguire, K., Suzuki, N., Tarlton, J. E., Pan, Y.-C., Bildsten, L., Fulton, B. J., Parrent, J. T., Sand, D.,

- Podsiadlowski, P., Bianco, F. B., Dilday, B., Graham, M. L., Lyman, J., James, P., Kasliwal, M. M., Law, N. M., Quimby, R. M., Hook, I. M., Walker, E. S., Mazzali, P., Pian, E., Ofek, E. O., Gal-Yam, A., & Poznanski, D. 2011, *Nature*, 480, 344
- Pakmor, R., Hachinger, S., Röpke, F. K., & Hillebrandt, W. 2011, *A&A*, 528, A117
- Pakmor, R., Kromer, M., Röpke, F. K., Sim, S. A., Ruiter, A. J., & Hillebrandt, W. 2010, *Nature*, 463, 61
- Perlmutter, S., Aldering, G., Goldhaber, G., Knop, R. A., Nugent, P., Castro, P. G., Deustua, S., Fabbro, S., Goobar, A., Groom, D. E., Hook, I. M., Kim, A. G., Kim, M. Y., Lee, J. C., Nunes, N. J., Pain, R., Pennypacker, C. R., Quimby, R., Lidman, C., Ellis, R. S., Irwin, M., McMahon, R. G., Ruiz-Lapuente, P., Walton, N., Schaefer, B., Boyle, B. J., Filippenko, A. V., Matheson, T., Fruchter, A. S., Panagia, N., Newberg, H. J. M., Couch, W. J., & The Supernova Cosmology Project. 1999, *ApJ*, 517, 565
- Raskin, C., Timmes, F. X., Scannapieco, E., Diehl, S., & Fryer, C. 2009, *MNRAS*, 399, L156
- Ricker, P. M. & Taam, R. E. 2008, *ApJ*, 672, L41
- Riess, A. G., Filippenko, A. V., Challis, P., Clocchiatti, A., Diercks, A., Garnavich, P. M., Gilliland, R. L., Hogan, C. J., Jha, S., Kirshner, R. P., Leibundgut, B., Phillips, M. M., Reiss, D., Schmidt, B. P., Schommer, R. A., Smith, R. C., Spyromilio, J., Stubbs, C., Suntzeff, N. B., & Tonry, J. 1998, *AJ*, 116, 1009
- Röpke, F. K., Hillebrandt, W., Schmidt, W., Niemeyer, J. C., Blinnikov, S. I., & Mazzali, P. A. 2007a, *ApJ*, 668, 1132
- Röpke, F. K., Woosley, S. E., & Hillebrandt, W. 2007b, *ApJ*, 660, 1344

- Rosswog, S., Kasen, D., Guillochon, J., & Ramirez-Ruiz, E. 2009, *ApJ*, 705, L128
- Saio, H. & Nomoto, K. 1998, *ApJ*, 500, 388
- . 2004, *ApJ*, 615, 444
- Seitenzahl, I. R., Meakin, C. A., Lamb, D. Q., & Truran, J. W. 2009a, *ApJ*, 700, 642
- Seitenzahl, I. R., Meakin, C. A., Townsley, D. M., Lamb, D. Q., & Truran, J. W. 2009b, *ApJ*, 696, 515
- Seitenzahl, I. R., Townsley, D. M., Peng, F., & Truran, J. W. 2009c, *Atomic Data and Nuclear Data Tables*, 95, 96
- Shen, K. J., Bildsten, L., Kasen, D., & Quataert, E. 2011, *ArXiv e-prints*
- Timmes, F. X. & Swesty, F. D. 2000, *ApJS*, 126, 501
- Timmes, F. X., Zingale, M., Olson, K., Fryxell, B., Ricker, P., Calder, A. C., Dursi, L. J., Tufo, H., MacNeice, P., Truran, J. W., & Rosner, R. 2000, *ApJ*, 543, 938
- Townsley, D. M., Bair, R. A., Dubey, A., Fisher, R. T., Hearn, N. C., Lamb, D. Q., & Riley, K. M. 2008, *Journal of Physics Conference Series*, 125, 012009
- Townsley, D. M., Calder, A. C., Asida, S. M., Seitenzahl, I. R., Peng, F., Vladimirova, N., Lamb, D. Q., & Truran, J. W. 2007, *ApJ*, 668, 1118
- van Kerkwijk, M. H., Chang, P., & Justham, S. 2010, *ApJ*, 722, L157
- Wang, L., Baade, D., Höflich, P., Wheeler, J. C., Kawabata, K., Khokhlov, A., Nomoto, K., & Patat, F. 2006, *ApJ*, 653, 490
- Wang, L., Baade, D., & Patat, F. 2007, *Science*, 315, 212
- Webbink, R. F. 1984, *ApJ*, 277, 355

- Weirs, G., Dwarkadas, V., Plewa, T., Tomkins, C., & Marr-Lyon, M. 2005, *Ap&SS*, 298, 341
- Whelan, J. & Iben, Jr., I. 1973, *ApJ*, 186, 1007
- Zel’dovich, Y. B., Librovich, V. B., Makhviladze, G. M., & Sivashinskii, G. I. 1970, *Journal of Applied Mechanics and Technical Physics*, 11, 264
- Zhu, C., Chang, P., van Kerkwijk, M., & Wadsley, J. 2011, *ArXiv e-prints*
- Zingale, M., Nonaka, A., Almgren, A. S., Bell, J. B., Malone, C. M., & Woosley, S. E. 2011, *ApJ*, 740, 8
- ZuHone, J., Ricker, P., Lamb, D., & Yang, H. 2008, in *Bulletin of the American Astronomical Society*, Vol. 40, *Bulletin of the American Astronomical Society*, 219–+

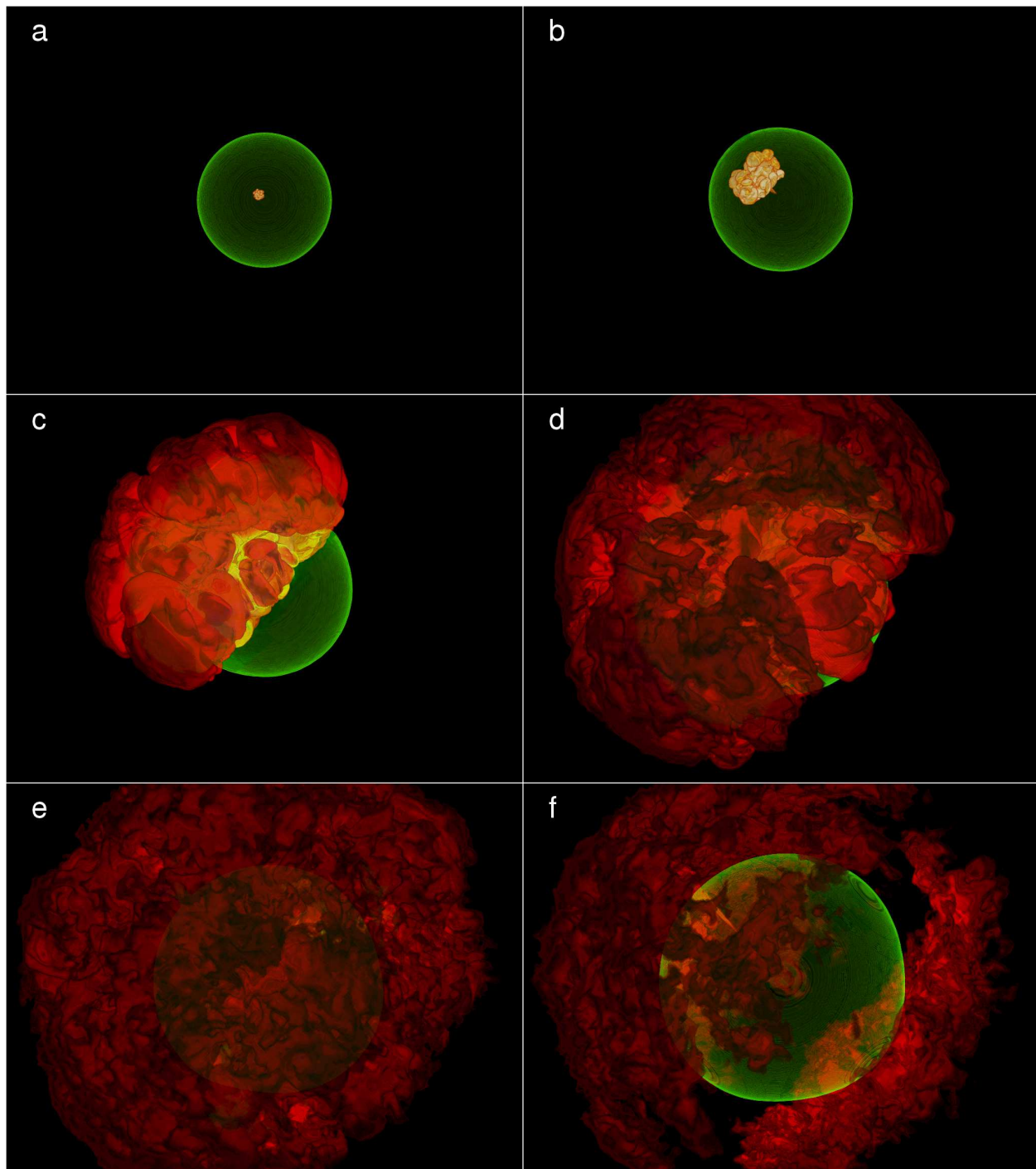


Fig. 1.— Six snapshots of the $63n128r168z$ simulation. The green contour approximates the location of the white dwarf surface. The range of orange colors are regions of high temperature. Bright orange is at the top end of the scale at 5×10^9 K and dark orange is at the bottom at 1×10^9 K. The high temperature regions consist primarily hot ash. The simulation time associated with each panel is: (a) 0.0 s, (b) 0.6 s, (c) 1.1 s, (d) 1.4 s, (e) 1.9 s, and (f) 2.2 s. Further discussion of this figure can be found in section 4.2.

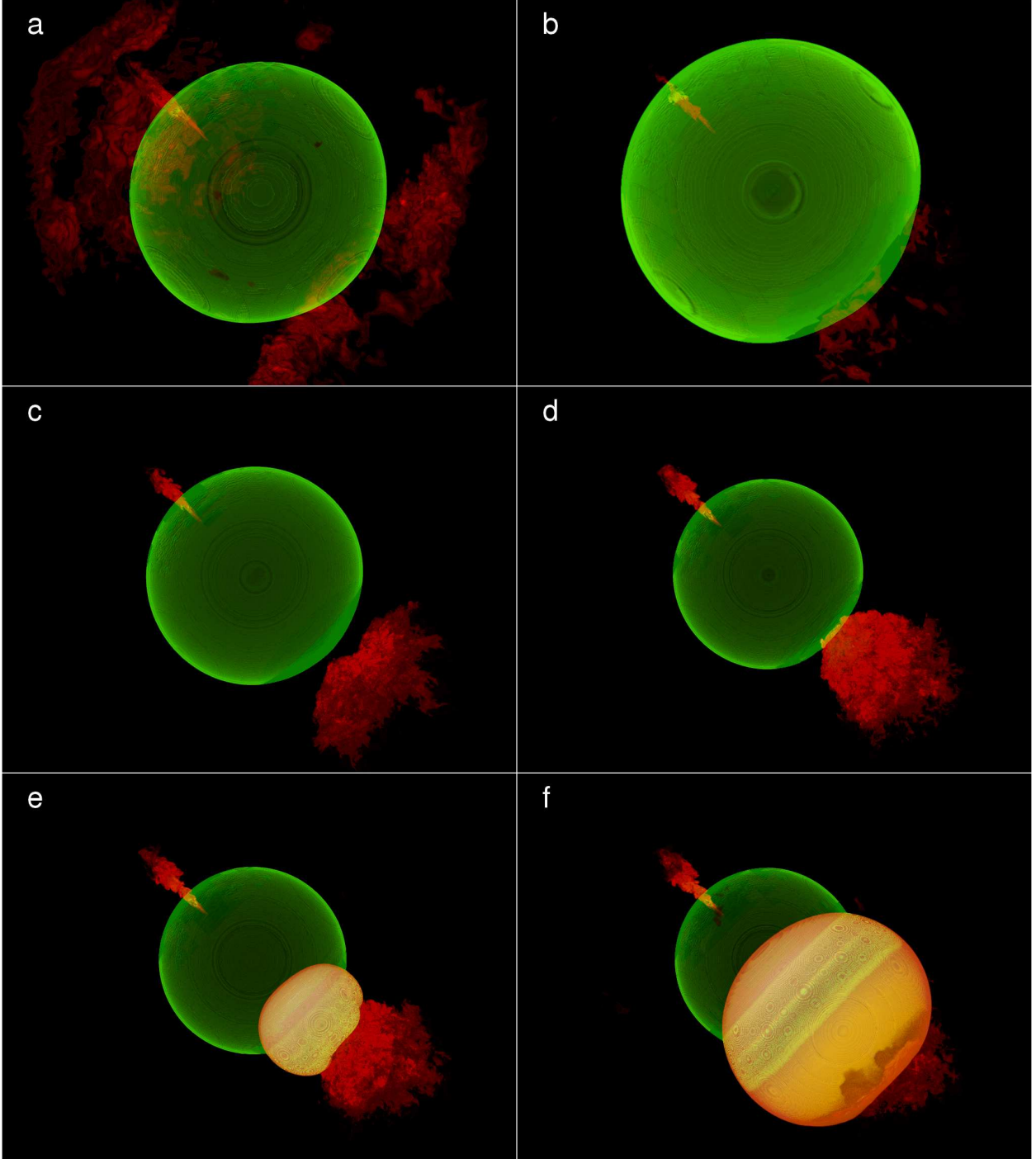


Fig. 2.— Six snapshots of the 63n128r168z simulation. The green contour approximates the location of the white dwarf surface. The range of orange colors are regions of high temperature. Bright orange is at the top end of the scale at 5×10^9 K and dark orange is at the bottom at 1×10^9 K. The high temperature regions consist primarily hot ash. The simulation time associated with each panel is: (a) 2.5 s, (b) 3.1 s, (c) 3.7 s, (d) 4.2 s, (e) 4.3 s, and (f) 4.4 s. Further discussion of this figure can be found in section 4.2.

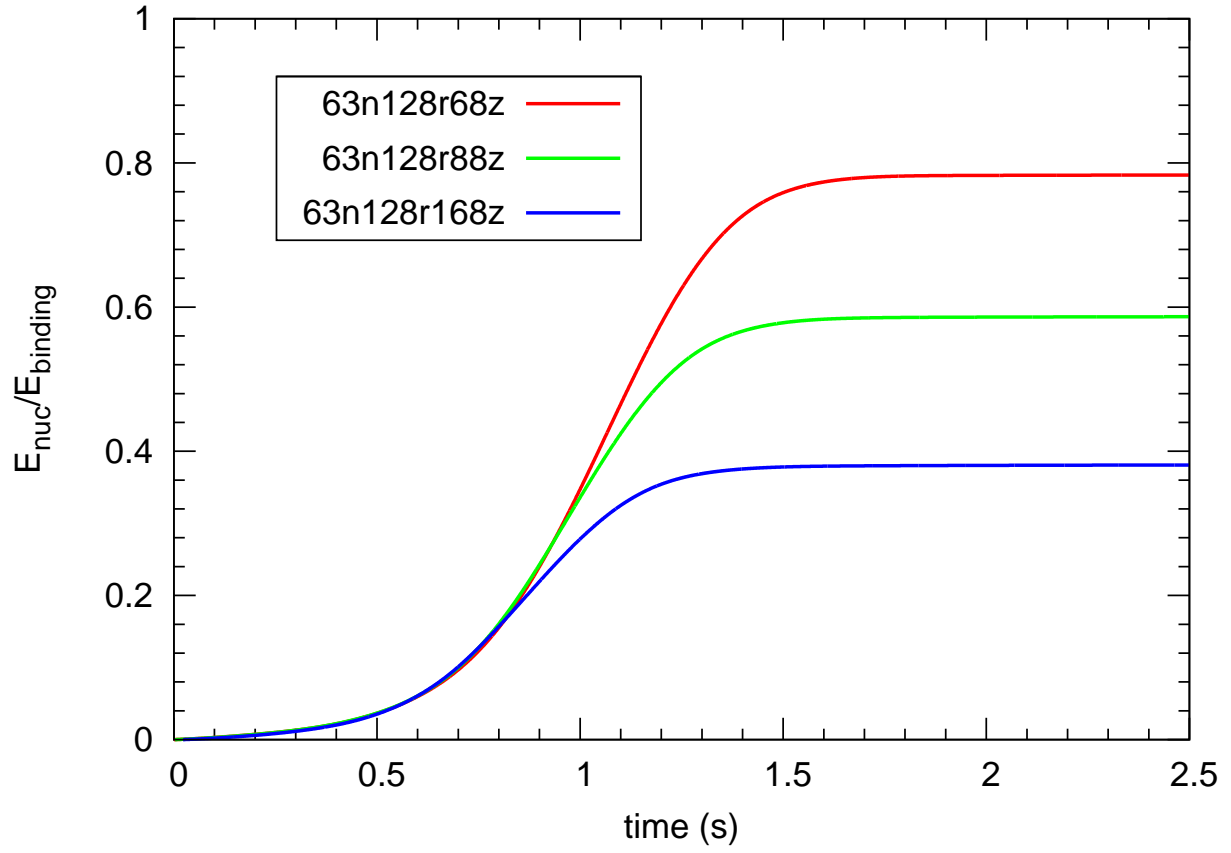


Fig. 3.— The fraction of binding energy increased due to nuclear energy input from the deflagration phase vs time for the three simulations.

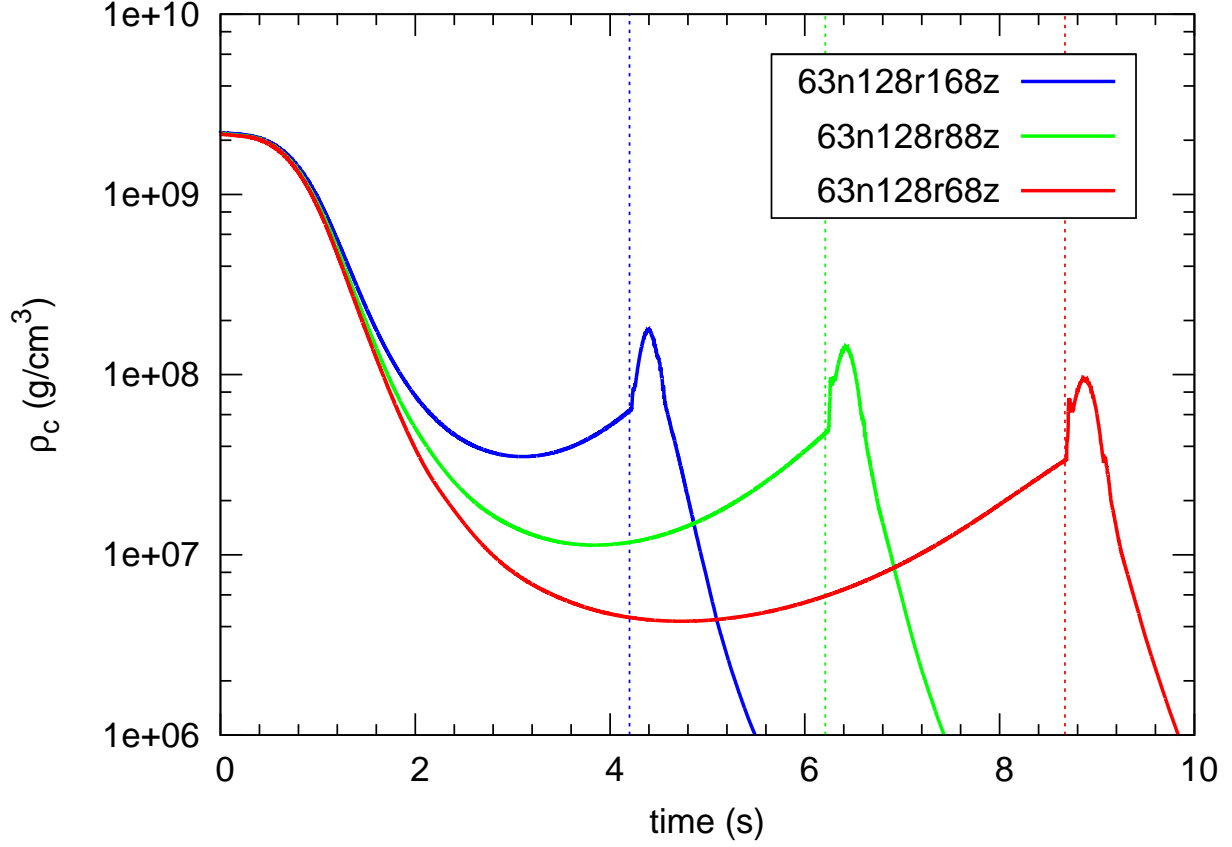


Fig. 4.— The central density, ρ_c , of the white dwarf vs time for the three simulations. This plot demonstrates the expansion and contraction of the white dwarf prior to detonation. The vertical lines mark the time at which a detonation occurred in each simulation.

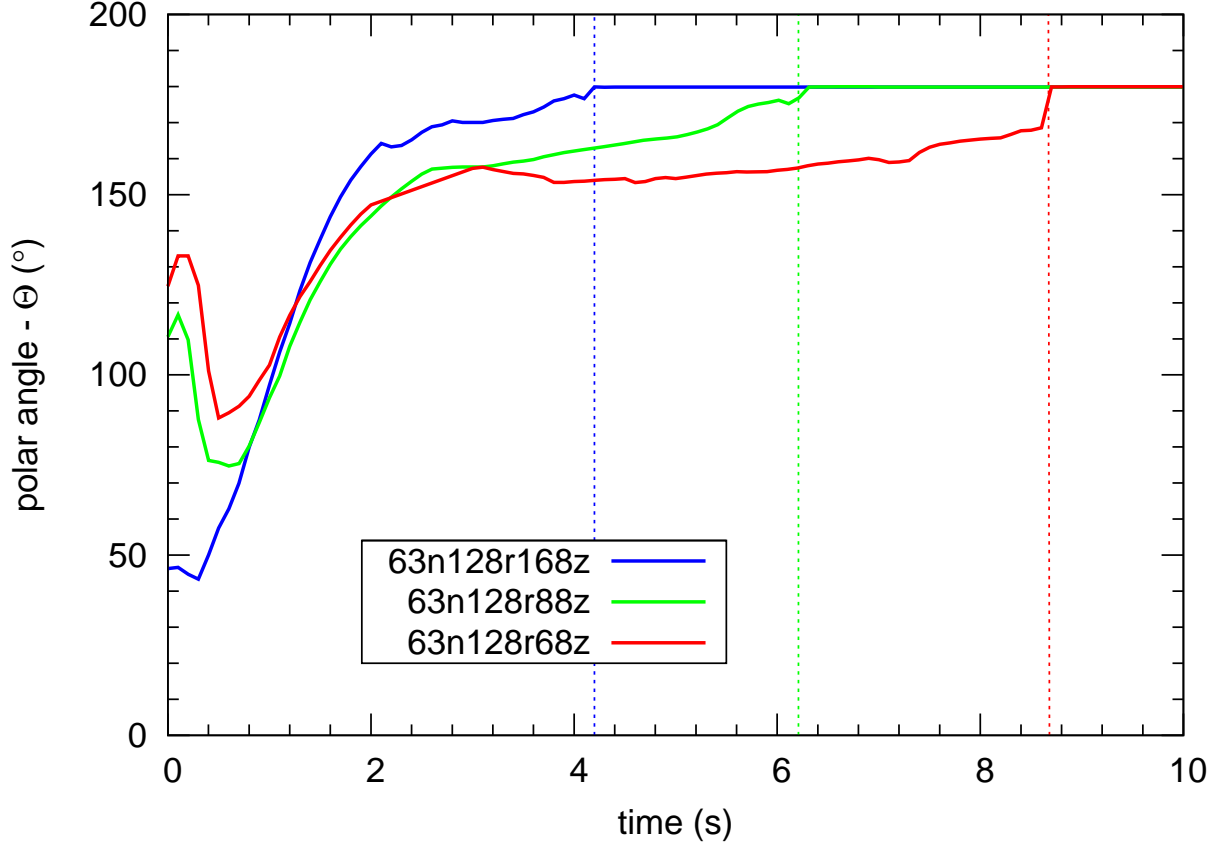


Fig. 5.— The polar angle, θ , of the leading edge of the ash vs time. This plot shows the progress of the fuel-ash mixture as it flows around the white dwarf. Note that the initially large polar angles during the first second of evolution is due to the flame burning into the lower hemisphere of the white dwarf. The vertical lines mark the time at which a detonation occurred in each simulation.

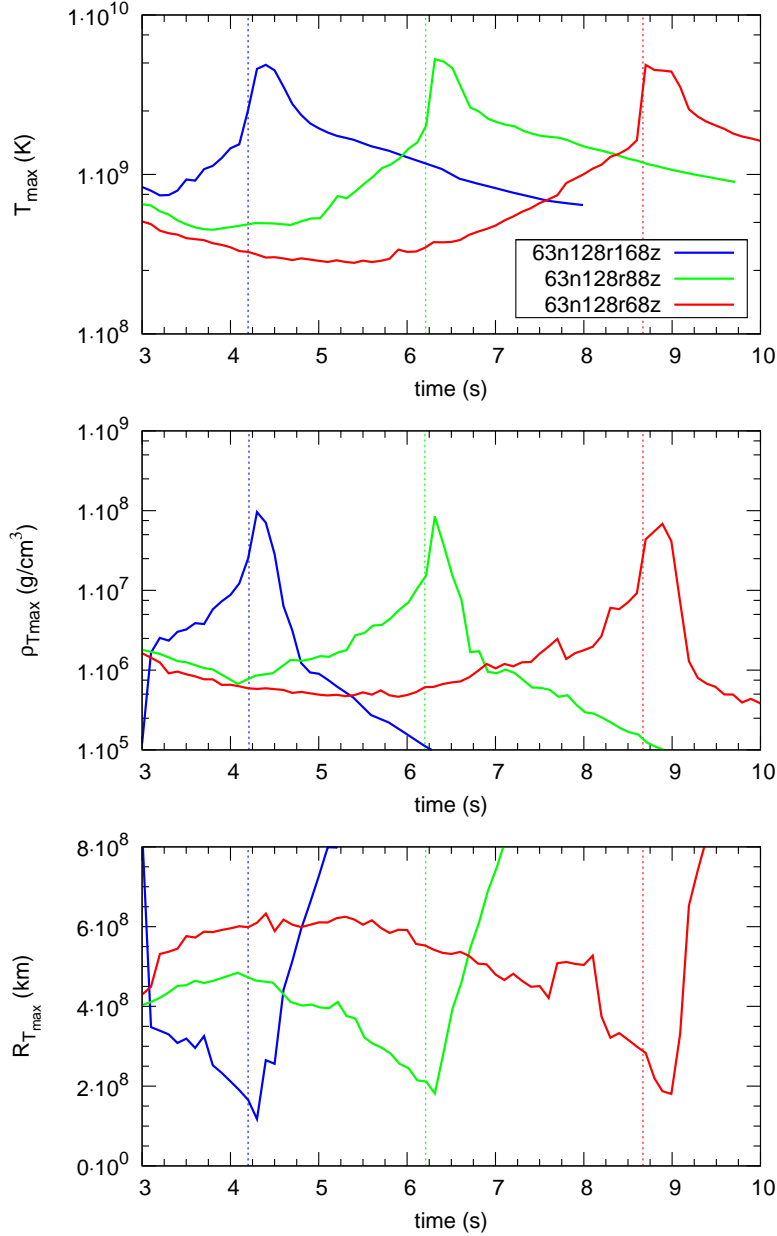


Fig. 6.— Conditions in the collision region: (*top*) The temperature of the computational cell with the maximum temperature in the collision region and whose material was composed of the fuel-ash mixture. The maximum temperature is plotted as a function of time. (*middle*) The density of the computational cell selected with the criteria described in the top figure as a function of time. (*bottom*) The radius of the computational cell selected with the criteria described in the top figure as a function of time. The vertical lines mark the time at which a detonation occurred in each simulation.

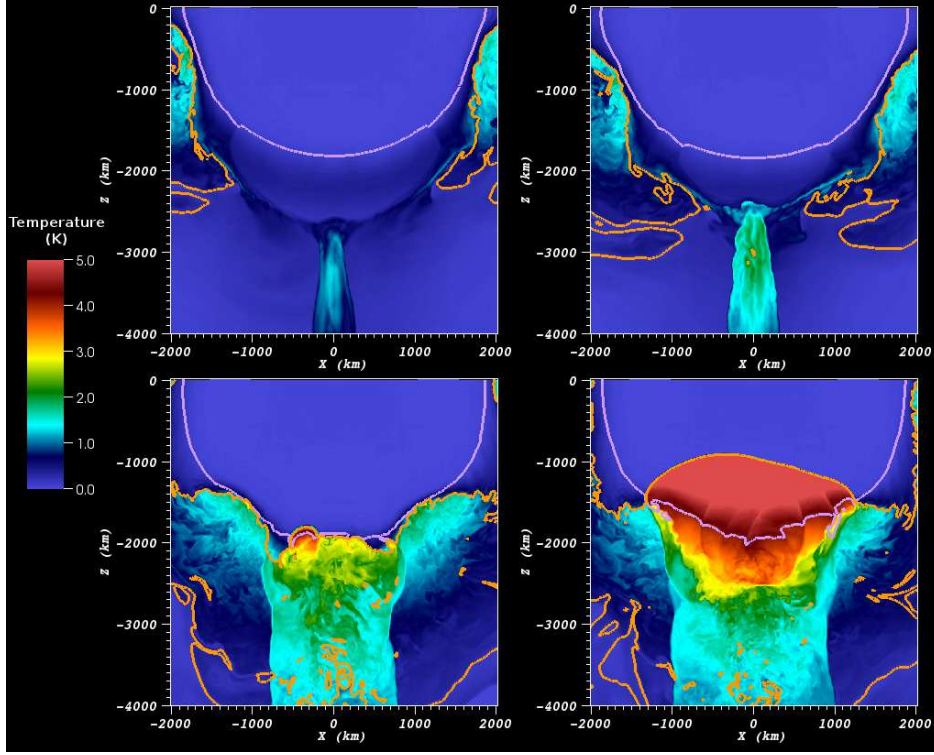


Fig. 7.— Slice images of the lead up to detonation of the classical GCD model of SNe Ia. This model is the *16b100o8r* detailed in J08. The four images are of the bottom hemisphere of the white dwarf. The slice plane is the x-z plane. The magenta contour is a density contour at $\rho = 1.0 \cdot 10^7$ g/cm³ - the nominal density at which hot C/O would detonate. The orange contour delineates material that is pure fuel from material that contains ash (e.g. ash that was converging on the collision region). The colors indicate temperature whose values correspond to the color bar on the left. The color bar is in units of 10^9 K. (*top left*) $t=1.8$ s. Ash approaches the collision region and a hot region forms. (*top right*) $t=1.9$ s. The ash converges further into the collision region. The hot region increases in temperature and begins to smolder. (*bottom left*) $t=2.22$ s. The smoldering fuel has pushed into the region with $\rho > 1.0 \times 10^7$ g/cm³ and a detonation has just formed. (*bottom right*) $t=2.3$ s. The detonation has spread from where it initially started. The high temperature region as well as the smooth detonation front is visible.

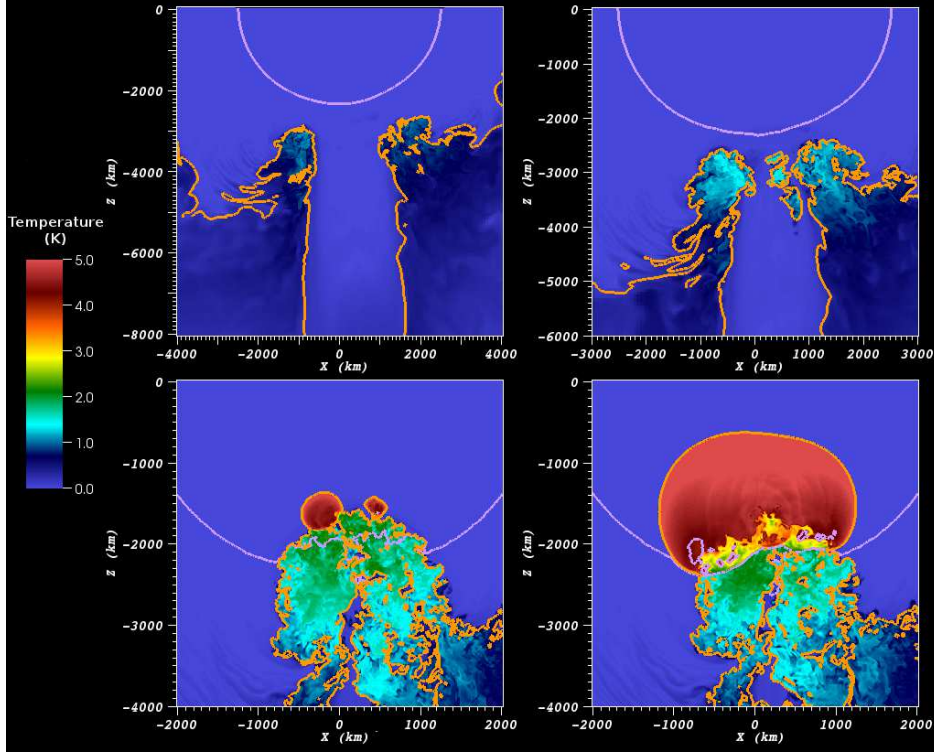


Fig. 8.— Slice images of the lead up to detonation of the pulsational GCD model of SNe Ia. This model is the $63n128r168z$. The four images are of the bottom hemisphere of the white dwarf. The slice plane is the x - z plane. The magenta contour is a density contour at $\rho = 1.0 \cdot 10^7 \text{ g/cm}^3$ - the nominal density at which hot C/O would detonate. The orange contour delineates material that is pure fuel from material that contains ash (e.g. ash that was converging on the collision region). The colors indicate temperature whose values correspond to the color bar on the left. The color bar is in units of 10^9 K . (*top left*) $t=3.5\text{s}$. Ash approaches the collision region. (*top right*) $t=3.8\text{s}$. Note that the figure is zoomed in from previous panel. The fuel-ash mixture continued to push into the collision region. The mixture heats since the white dwarf was contracting and the ash was pushing to higher densities (*bottom left*) $t=4.23\text{s}$. Note that the figure is zoomed in from the previous panel. The mixture has reached the critical temperature and density and a detonation has just formed at several locations in the mixture. (*bottom right*) $t=4.3\text{s}$. The detonation wave is spreading through the star. The high temperature region behind the detonation wave as well as the smooth detonation front are clearly visible.

Table 1. List of simulations and their properties

sim name	Δx^a (km)	n_{ign}^b	r_{ign}^c (km)	z_{ign}^d (km)	$E_{nuc,def}^e$ (10^{49} ergs)	$E_{nuc,def}^f$ ($E_{binding}$)	$\rho_{c,min}^g$ (10^7 g/cm ³)	$t_{\rho_{c,min}}^h$ (s)	t_{det}^i (s)	R_{det}^j (km)	$E_{kinetic}^k$ (10^{51} ergs)
63n128r168z	8	63	128.0	168.0	18.9	0.38	3.51	3.10	4.20	1,630	1.23
63n128r88z	8	63	128.0	88.0	29.1	0.59	1.13	3.83	6.21	2,124	1.19
63n128r68z	8	63	128.0	68.0	38.6	0.78	0.43	4.71	8.67	2,660	1.05

^aMaximum spatial resolution of the simulation.

^bNumber of ignition points.

^cRadius of the spherical volume containing the ignition points.

^docation along the z-axis of the origin of the spherical volume containing the ignition points.

^eAmount of energy released during the deflagration phase.

^fAmount of energy released during the deflagration phase as a fraction of the binding energy of the white dwarf.

^gCentral density of the white dwarf at maximum expansion.

^hTime at which the white dwarf reaches maximum expansion.

ⁱTime at which the white dwarf detonates.

^jRadius of the location where the detonation is initiated in the white dwarf.

^kKinetic energy contained in post-explosion nebula.

Table 2. Final yields from simulations with multiple ignition points.

sim name	X(^{12}C)	X(^{16}O)	X(^{24}Mg)	X(Si-group)	X(NSE)
	M_{\odot}	M_{\odot}	M_{\odot}	M_{\odot}	M_{\odot}
63n128r168z	0.064	0.099	0.030	0.19	0.98
63n128r88z	0.091	0.14	0.045	0.20	0.89
63n128r68z	0.13	0.19	0.062	0.27	0.72

Table 3. Deflagration products of simulations with multiple ignition points.

sim name	X(^{24}Mg)	X(Si-group)	X(NSE)
	M_{\odot}	M_{\odot}	M_{\odot}
63n128r168z	0.017	0.025	0.086
63n128r88z	0.022	0.033	0.142
63n128r68z	0.030	0.044	0.190